ELSEVIER

Journal of Alloys and Compounds 404–406 (2005) 7–15

Journal of ALLOYS AND COMPOUNDS

www.elsevier.com/locate/jallcom

The structure and phase diagram of M–H systems at high chemical potentials—High pressure and electrochemical synthesis

Y. Fukai*

Department of Physics, Chuo University, Kasuga, Bunkyo-ku, Tokyo 112-8551, Japan

Received 2 September 2004; received in revised form 8 February 2005; accepted 14 February 2005
Available online 15 July 2005

Abstract

Efforts to provide a unified picture of metal–hydrogen alloys over a wide range of chemical potentials are described. High chemical potentials are produced either by high-pressure molecular hydrogen or high excess potentials in electrolytic charging or electrodeposition. General systematics of the phase diagram of 3d-metal–hydrogen systems are noted; a drastic reduction of the melting point and the stabilization of close-packed structures with dissolution of hydrogen. Supercritical anomalies are observed in the fcc phase of Fe–H, Co–H and Ni–H systems. In the electrodeposition of metals, it is shown that structural changes are caused by dissolution of hydrogen, and superabundant vacancies of concentrations $\sim 10^{-4}$ are present.

Keywords: Metal–hydrogen systems; Phase diagram; High pressure; Electrodeposition; High chemical potential

1. Introduction

For a complete description of the constitution of M–H systems, experiments must be performed over wide ranges of thermodynamic variables; the composition from pure metal to pure hydrogen, the temperature from absolute zero to above the melting point of constituent metals and the pressure up to, say, 10 GPa. To perform such experiments on many different metals, having widely different affinities to hydrogen, we must be able to determine structures up to high chemical potentials of hydrogen, namely up to high hydrogen pressures or high excess voltages in electrochemical charging. One of the common problems encountered in such experiments is to achieve thermodynamical equilibrium between the M–H sample and surrounding hydrogen environment. It happens frequently that surface barrier hinders the equilibrium hydrogen concentration to be attained. In such cases, seal-off type experiments dealing with samples of prescribed hydrogen concentrations should be performed. Another problem is the formation of superabundant vacancies (SAVs). It has come to be recognized that the most stable structure of all M–H systems is the one containing a large number of M-atom vacancies, i.e. superabundant vacancies—more precisely, vacancies with several interstitial hydrogen atoms trapped (Vac-H clusters) [1]. However, the formation of such defect structures usually requires high temperatures, high hydrogen pressures and long holding times—the conditions hardly realized in ordinary experiments. Thus, in ordinary methods of sample preparation, only meta-stable structures without containing M-atom vacancies can be formed. All the phase diagrams of M–H systems reported to date are in this sense meta-stable ones. The only possible exception is electrodeposited metals where the most stable structure composed of H and M-atoms and their vacancies can be built from the very beginning [4]. This problem will be described in Section 4.

2. Chemical potential of hydrogen

It may be expedient here to review some features of the chemical potential of molecular hydrogen at high pressures and of hydrogen ions in solution at high excess voltages.

* Tel.: +81 3 3817 1769; fax: +81 3 3817 1792.
E-mail address: fukai@phys.chuo-u.ac.jp (Y. Fukai).

0925-8388/$ – see front matter © 2005 Elsevier B.V. All rights reserved.
doi:10.1016/j.jallcom.2005.02.075

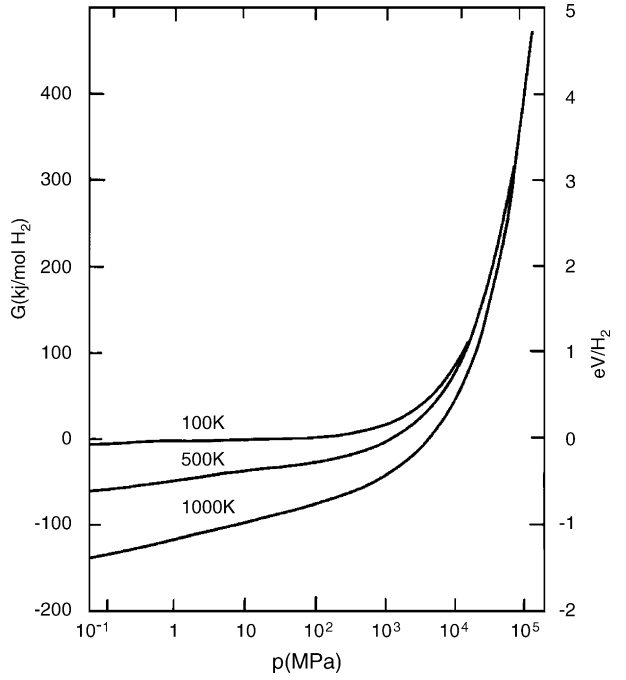

Fig. 1. The chemical potential of molecular hydrogen H_2 as a function of p and T [3–5].

Fig. 1 shows the chemical potential of molecular hydrogen μ_{H_2} as a function of hydrogen pressure p_H, at several different temperatures [3–5]. A notable feature is a break at $p_H \sim 1$ GPa, followed by a steep increase thereafter. Below the break, straight lines with slopes proportional to temperature represent the variation according to the ideal-gas formula. Above the break, a sharp rise independent of temperature is caused by strong intermolecular (repulsive) interactions. From this variation of the chemical potential, we may expect that the response of M–H samples to surrounding hydrogen should be very different at pressures below or above $p_H \sim 1$ GPa.

This expectation is borne out by the enhanced solubilities over the ideal-gas formula (Sievertz law) at $p_H \geq 1$ GPa. As an example, the solubility calculated for γ(fcc)-Fe is shown in Fig. 2 [4,5]. On this Arrhenius plot, the solubility below $p_H \sim 0.1$ GPa roughly follows the Sievertz law (the ideal-gas behavior), whereas above $p_H \sim 1$ GPa its increase with pressure becomes more pronounced. Thus in many M–H systems, high hydrogen concentrations and new high-pressure phases are realized at $p_H \geq 1$ GPa.

In electrolytic charging, on the other hand, a sample constituting a cathode is placed in contact with a solution in which the chemical potential of hydrogen ions, μ_{H^+} is raised by application of excess voltage V:

$$\mu_{H^+} = \mu^0_{H^+} + eV,$$

where $\mu^0_{H^+}$, the zero of the potential, is usually taken to be equal to Standard Hydrogen Electrode (SHE), in equilibrium with gaseous hydrogen under normal conditions (equal to

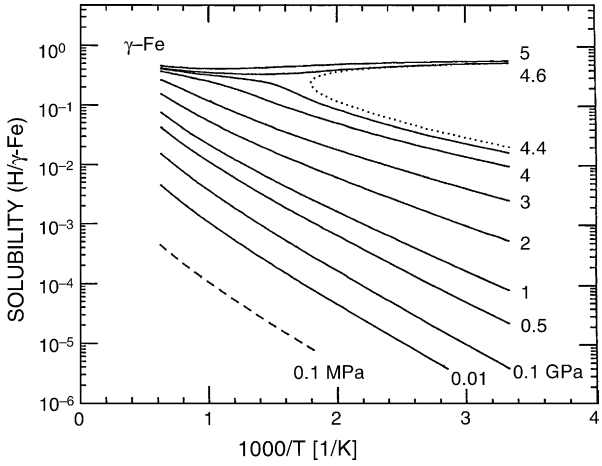

Fig. 2. The solubility of H in γ-Fe as a function of p_H and T [4,5].

$1/2\mu_{H_2}$ at 0.1 MPa (1 atm) and room temperature), and e is the electron charge. A diagram for converting the excess voltage to equivalent pressure of molecular hydrogen at room temperature can be readily constructed from the above calculations, as shown in Fig. 3.

Here, a word of caution is in order against the misuse of "fugacity", which is rather prevalent in electrochemistry. The fugacity f is defined as a fictitious pressure of ideal gas, related to the excess voltage by

$$\frac{1}{2}kT \ln f = eV.$$

As shown by a broken line in Fig. 3, the fugacity agrees with the actual pressure of molecular hydrogen only at low pressures, $p_H < 0.1$ GPa (10^3 atm). The deviation becomes really formidable above 0.1 GPa. The fugacity corresponding to the excess voltage of 0.2 V is stunning 780 GPa, whereas the actual equivalent pressure is 1 GPa. It is, there-

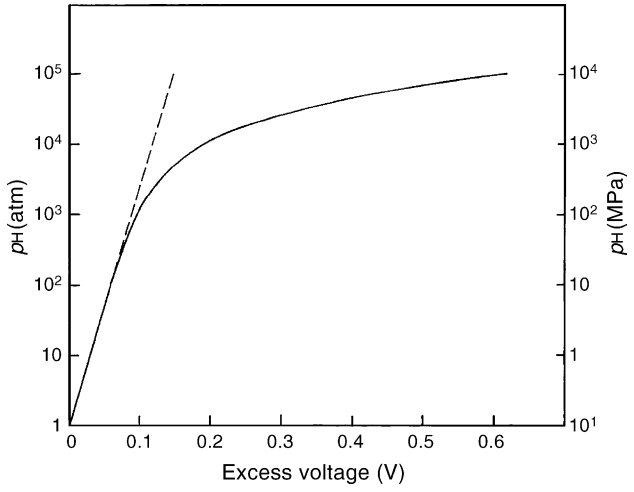

Fig. 3. The pressure of molecular hydrogen H_2 (p_H) in equilibrium with ionic hydrogen H^+ in solution under application of the excess voltage V. The zero of the potential is taken at SHE (0.1 MPa (1 atm) of H_2 gas at room temperature). The dashed line shows the fugacity as a function of V.

fore, strongly advised not to use "fugacity" at pressures higher than ∼0.1 GPa (the excess voltage of ∼ 0.1 V). A strong deviation of molecular fluid hydrogen from ideal-gas makes the notion of fugacity physically meaningless.

3. Phase diagrams of M–H alloys at high hydrogen pressures and temperatures

Studies of equilibrium p_H, T conditions for hydride formation were initiated by a Polish group in 1960s, by compressing gaseous hydrogen to $p_H \sim 1.5$ GPa at $T \leq 450\,^\circ$C. See the review paper [6]. Subsequently, a Russian group developed a technique of producing higher hydrogen pressures by decomposition of some hydrogen-containing material inside an externally compressed cell. Also, by developing a technique to recover specimens from the high-pressure cell by cooling to liquid N_2 temperature before decompression, they determined the structure and hydrogen concentrations of hydrides synthesized under high hydrogen pressures. Their p_H and T conditions ranged between $p_H \leq 9$ GPa and $-150\,^\circ\text{C} \leq T \leq 500\,^\circ$C, and more recently up to $p_H \leq 3$ GPa and $T \leq 900\,^\circ$C. The results of their investigation of a series of 3d- and 4d-metal hydrogen systems are reviewed in Refs. [7,8].

We developed a technique of hydriding samples over wider ranges of p_H, T conditions; 2 GPa $\leq p_H \leq$ 10 GPa and $T \leq 1200\,^\circ$C, which also allowed in situ XRD measurements using synchrotron-radiation X-rays. Details of our experimental techniques were described elsewhere [9,10]. As shown below, in situ measurements proved very useful in investigating the kinetics of the phenomena occurring under high p_H and T conditions.

Here we confine ourselves to 3d transition metals, and try to demonstrate some general trends in the phase diagrams of M–H systems across the series, from Sc to Ni, primarily based on our recent experiments.

The structure of the host metal varies from hcp (Sc and Ti), through bcc (Ti, V, Cr and Mn) to fcc (Fe, Co and Ni), with other allotropic structures in Mn, Fe and Co stabilized by magnetism.

For Sc, Ti and V, which form stable hydrides, seal-off type experiments were performed, and x–T (composition–temperature) diagrams were constructed.

In the Sc–H system, in addition to the extended solid-solution phase α^* (with hydrogen atoms forming H–Sc–H pairs along the c-axis), and a dihydride phase of CaF_2 structure, a hexagonal trihydride phase ($ScH_{2.65}$) was formed under high hydrogen pressure ($p_H = 1.0$ GPa) [11]. These features are in line with other lanthanide–H systems. For lanthanide–H systems, see the review paper by Vajda [12].

The phase diagram (x–T diagram) of the Ti–H system, determined at $p_H \leq 30$ MPa, is shown in Fig. 4 [13,14]. This was in fact the first case where the large melting point reduction was observed (though not recognized as such) [13]. This diagram changes at $p_H \geq 2$ GPa, as a new phase ζ appears at $x \approx 0.7$ [15], as shown in Fig. 5 [16]. This phase has a bct structure isomorphous with the β phase of the V–H system (see below). In addition, there is an indication that a trihydride phase is formed at $p_H \geq 5$ GPa. The phase relation above the trihydride composition is largely a speculation (except the melting point of elemental hydrogen [17]). In view of the difference of bonding character, a miscibility gap must exist between the M–H alloys and elemental hydrogen, both in solid and liquid states.

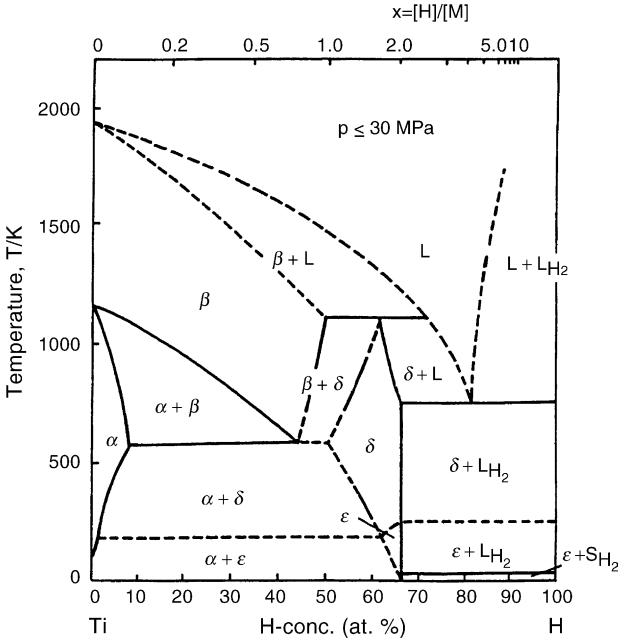

Fig. 4. The x–T diagram of the Ti–H system at pressures less than 30 MPa [13,14].

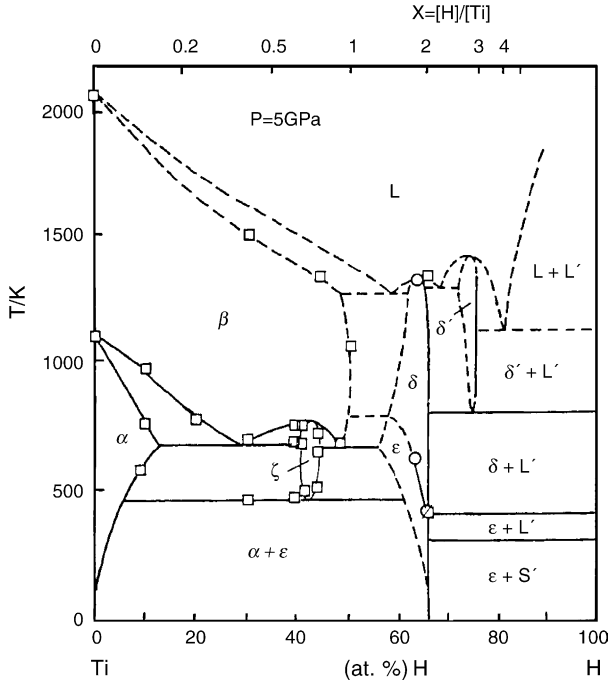

Fig. 5. The x–T diagram of the Ti–H system at pressures at 5 GPa [16].

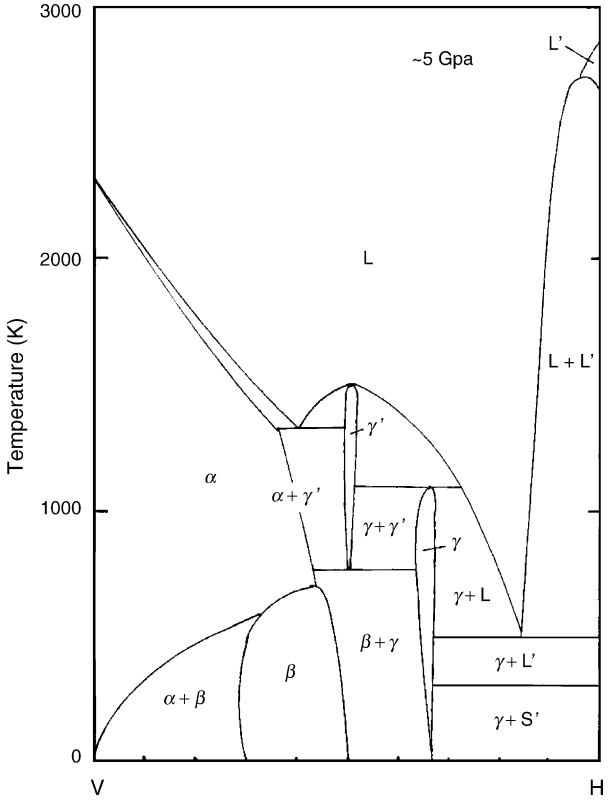

Fig. 6. The x–T diagram of the V–H system at pressures at ∼5 GPa [18].

The phase diagram of the V–H system at $p_H \sim 5$ GPa is shown in Fig. 6 [18]. A peculiar feature is the appearance of a high-pressure phase γ, which is a monohydride phase having a very high melting point. In effect, there are two fcc phases occurring at high pressures; γ(VH) and γ'(VH_2). The bct phase ($VH_{0.5}$) is stabilized relative to the α(bcc) phase at high pressures due to smaller H-induced volume on O_z sites in comparison to T sites in the α phase [19]. There is an indication that at high H concentrations around 85 at.% H, a liquid phase persists to rather low temperatures, forming an invariant line at ∼ 500 K. This suggests an interesting possibility that a liquid alloy with a small amount of V dissolved in metallic hydrogen solvent can be synthesized.

From Cr to Ni, structure determinations were made by in situ XRD at high temperatures and high hydrogen pressures. The p_H –T diagrams thus obtained are shown in Fig. 7 for the Cr–H system [20], Fig. 8 for the Mn–H system [21], Fig. 9 for the Fe–H system [22], Fig. 10 for the Co–H system [23] and Fig. 11 for the Ni–H system [24,25]. The following general trends can be noticed.

(1) The melting point is lowered appreciably with dissolution of hydrogen, reaching a minimum at $p_H = 2$–3 GPa.
(2) Transitions to close-packed structures take place at $p_H =$ 1–2 GPa, in the order of hcp→dhcp→fcc with increasing temperature. In all the pressure-induced hcp and dhcp phases, the axial ratio was found to assume very nearly the ideal value.

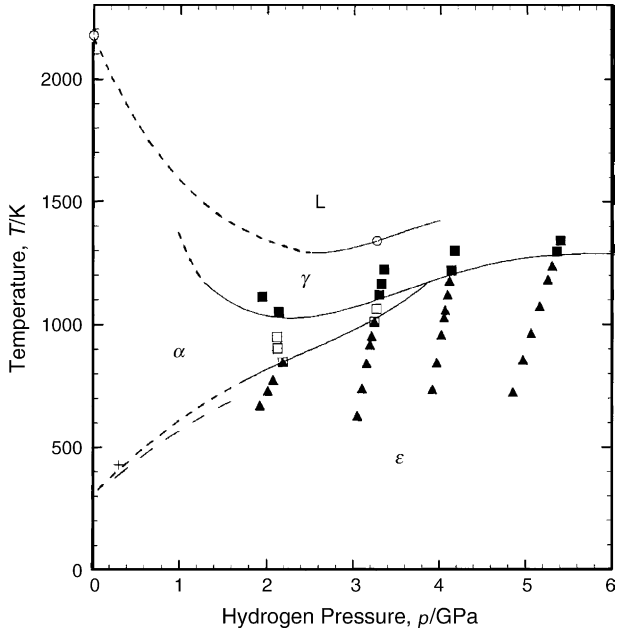

Fig. 7. The p_H–T diagram of the Cr–H system [20]. The $\alpha - \varepsilon$ boundary determined earlier in the lower p_H, T region [7] is also inscribed.

(3) The fcc structure tends to be favored to the right of the 3d series.

In the Fe–H and Ni–H systems, conversion to x–T diagrams was made by estimating the hydrogen concentration from observed lattice expansions, assuming appropriate values for the H-induced volume, $v_H = 2.3$ Å^3 for H in γ(fcc)-Fe and $v_H = 2.2$ Å^3 for H in Ni. Results are shown in Fig. 12 for the Ni–H system [24,25] and Fig. 13 for the Fe–H system [26], respectively. In the Ni–H system, where the struc-

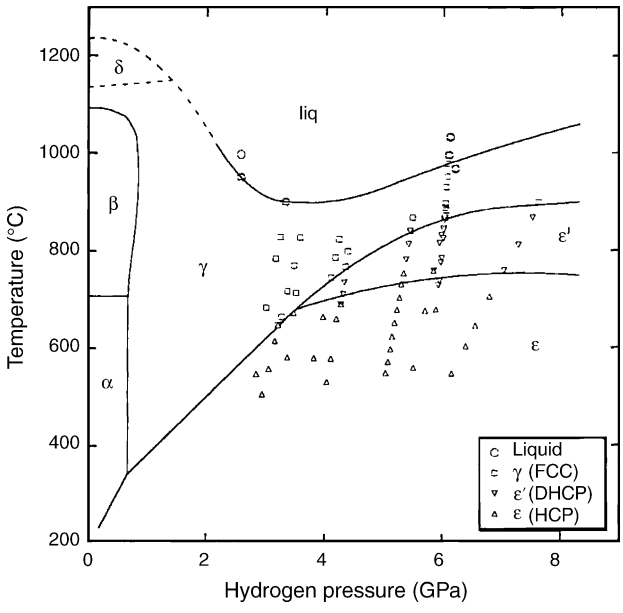

Fig. 8. The p_H–T diagram of the Mn–H system [21].

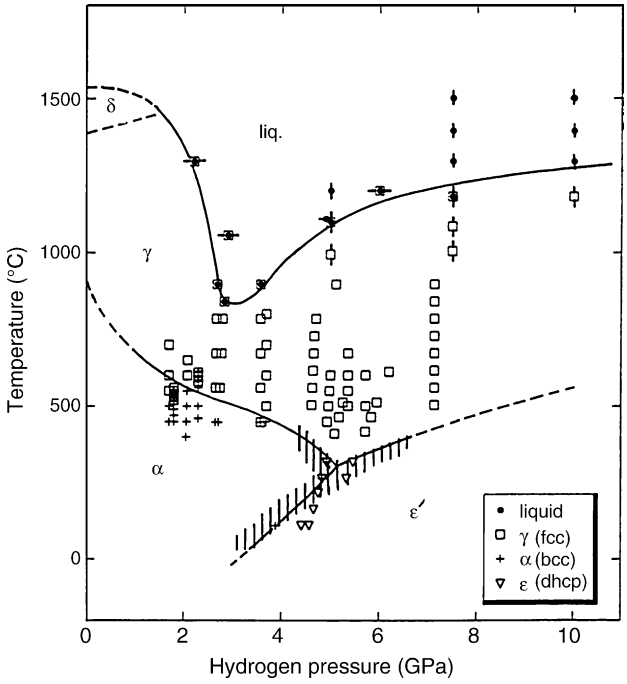

Fig. 9. The p_H–T diagram of the Fe–H system [22]. The dashed area represents the region of the earlier data [7].

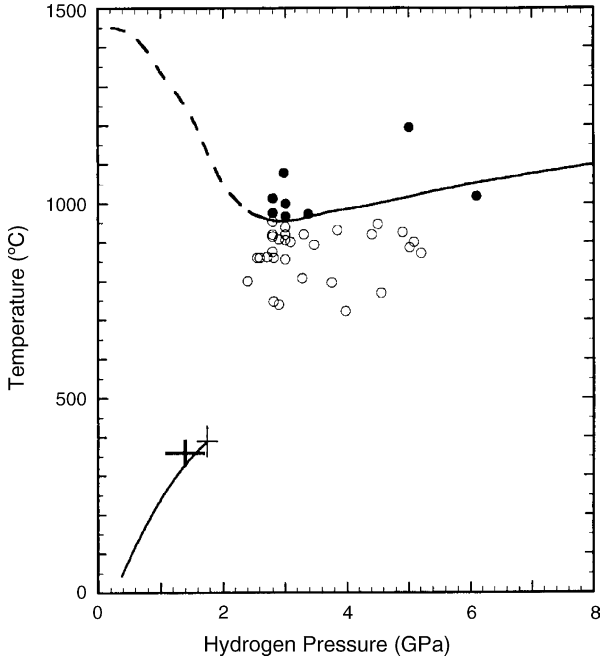

Fig. 11. The p_H–T diagram of the Ni–H system [24,25]. The boundary of two-phase coexistence region and a critical point with thin error bars are taken from [7], and a critical point with thick error bars from [24,25].

ture is always fcc, the spinodal decomposition takes place, with a critical point located at $p_c \approx 1.4$ GPa, $T_c \approx 360\,^\circ$C. In the γ(fcc) phase of the Fe–H system (Fig. 13), the dissolution process changes with pressure from endothermic to exothermic at $p_H \sim 5$ GPa, which is a typical behavior in the supercritical region. The critical point, roughly located at $p_c \approx 4.5$ GPa and $T_c = 400 \pm 100\,^\circ$C, is close to the α–γ phase boundary, and is therefore hard to determine accurately. (Note that the observed result agrees reasonably well with the calculation shown in Fig. 2.) The supercritical anomaly similar to Figs. 12 and 13 was also observed in the Co–H system, and a hypothetical critical point was roughly located at $p_c = 5.5$–6 GPa and $T_c \leq 300\,^\circ$C, which is actually in the hcp region [23].

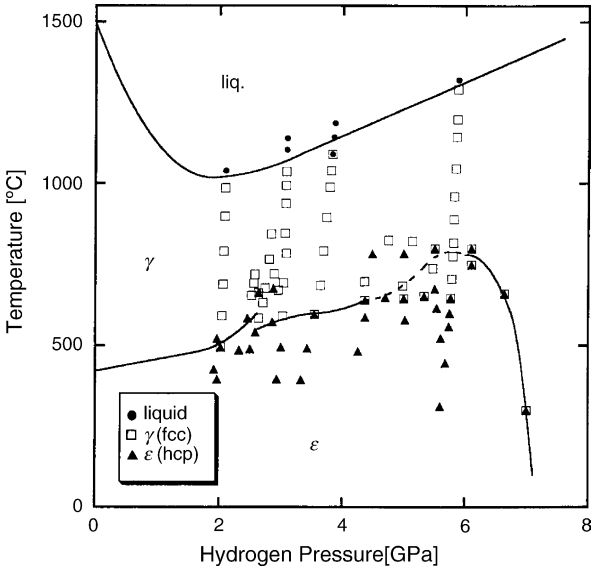

Fig. 10. The p_H–T diagram of the Co–H system [23].

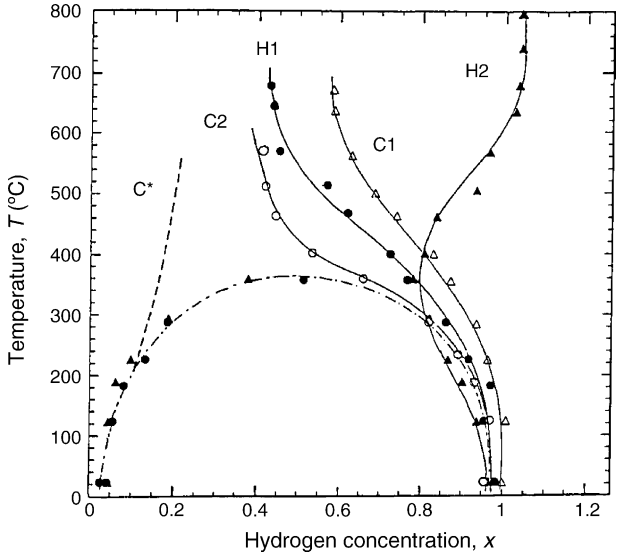

Fig. 12. The x–T diagram of the Ni-H system [24,25]. Heating runs H1 and H2, and cooling runs C1 and C2. Actual pressures in each run at room temperature, ~400 °C and the highest temperatures are H2 (4.3–4.6–5.4 GPa), C1(1.5–2.1–2.4 GPa), H1(1.9–2.1–2.2 GPa), and C2(1.1–1.4–2.1 GPa), respectively. An isobar labeled C* illustrates (schematically) the expected temperature dependence at a lower pressure (≤1 GPa).

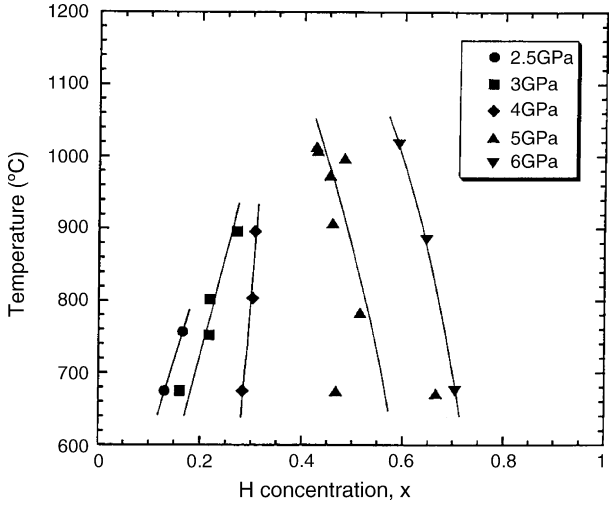

Fig. 13. The x–T diagram of the γ–Fe–H system [26].

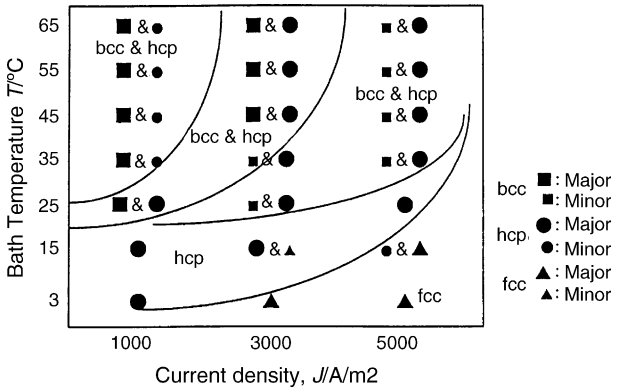

Fig. 14. The structure of electrodeposited Cr films as a function of current density and temperature. The deposition was made on an amorphous Ni–P substrate [28].

4. Structure of electrodeposited metals

It has been widely recognized that electrodeposited metals often assume structures different from ordinary ones [27]. In Cr, for example, electrodeposited films often assume hcp and/or fcc structures, instead of ordinary bcc. The mechanism of appearance of these different structures has not been understood.

Anticipating that the electrodeposition should dissolve hydrogen in metals, we performed critical experiments on Cr to determine the structure as a function of temperature and current density. If hydrogen is a major cause of producing different structures, we may thus obtain the phase relation equivalent to the x–T diagram. The results obtained for Cr is shown in Fig. 14 [28]. The electrodeposition was made on an amorphous Ni–P substrate, and structure determination was made immediately after the deposition. The diagram shows that the film assumes the ordinary bcc structure at low current densities and high temperatures, the hcp structure under intermediate conditions, and the fcc structure at high current densities and low temperatures. This is the order of increasing hydrogen concentration, as was verified by thermal desorption measurements. Even admitting some ambiguities arising from possible loss of hydrogen and concomitant structural changes after deposition, we may conclude that hydrogen is primarily responsible for the observed structural variations.

It is desirable in theory to perform in situ determination of structure as a function of excess voltage and temperature, in order to allow detailed comparison with p_H–T diagrams obtained from high p_H and T experiments.

5. Effects of superabundant vacancy formation

One of the characteristic features of the formation of superabundant vacancies is that their equilibrium concentration attains the highest value in the fcc structure in comparison

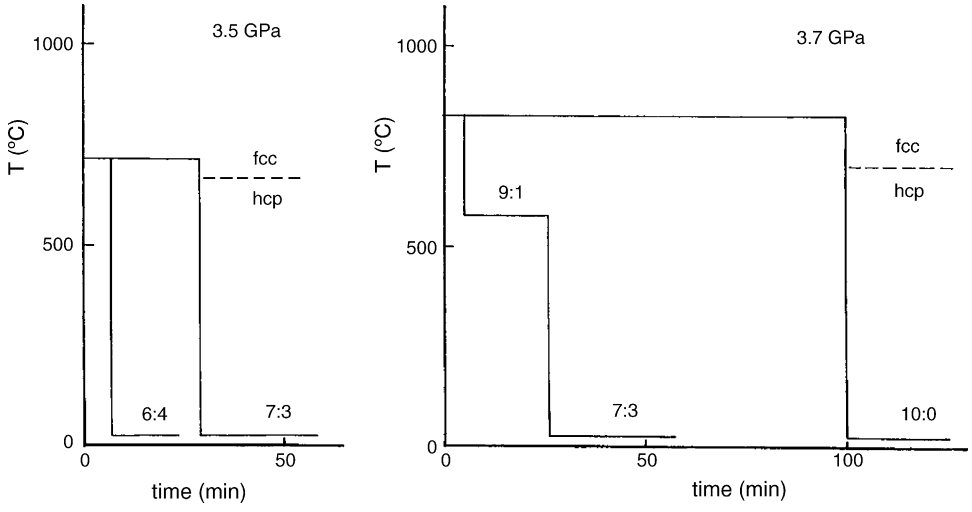

Fig. 15. The effect of SAV formation on the phase stability of Mn–H alloys. The retained fcc fraction after cooling from fcc to hcp region is measured as a function of holding time in the fcc phase. The observed fractions are inscribed as fcc:hcp.

to bcc and hcp structures. Naturally, the formation of SAVs in turn stabilizes the fcc structure relative to bcc and hcp structures.

This effect is clearly demonstrated in the Mn–H system, as shown in Fig. 15. Whereas the transition ε(hcp)–ε'(dhcp) is completely reversible, the transition ε'(dhcp)–γ(fcc) is not. The transition $\varepsilon' \rightarrow \gamma$ occurs instantly on crossing the phase boundary, but the occurrence of the reverse transition $\gamma \rightarrow \varepsilon'$ depends on the holding time in the γ phase. After sufficiently long holding times ($\geq$2 h), the fcc structure became very stable and remained as such even after recovery to ambient conditions. This dependence on the holding time can be taken to be the manifestation of the effect of SAV formation on the stability of the γ phase.

This reasoning is supported by comparison of the stabilizing time of the γ phase with the time needed for the introduction of SAVs. Assuming that Vac-H clusters are introduced by diffusion from the surface, and estimating the diffusivity in the fcc lattice from the expression derived for the Pd–H alloy, $D_{\mathrm{cl}} = 3.8 \times 10^{-4}\,\mathrm{e}^{-(1.20+0.050p(\mathrm{GPa}))\mathrm{eV}/kT}\ \mathrm{cm}^2/\mathrm{s}$ [29], which becomes $10^{-10}\ \mathrm{cm}^2/\mathrm{s}$ for the experimental condition $p = 3.7$ GPa and $T = 1073$ K, we obtain a time needed for diffusion over the particle size of 10 μm equal to $\sim$ 20 min. This is of the same order of magnitude as the observed time for stabilization of the γ phase in the Mn–H system.

It may be anticipated that, even at room temperature, the introduction of SAVs may not be totally negligible. The diffusivity of a Vac-H cluster in Pd cited above, equal to $3 \times 10^{-24}\ \mathrm{cm}^2/\mathrm{s}$ at room temperature, gives in fact a lower bound of the diffusivity corresponding to the maximum occupancy of H atoms (6 per vacancy); the upper bound is given by that of a bare vacancy, $D_{\mathrm{v}} = 0.1\mathrm{e}^{-1.03\mathrm{eV}/kT}\ \mathrm{cm}^2/\mathrm{s}$ [30], equal to $4 \times 10^{-19}\ \mathrm{cm}^2/\mathrm{s}$ at room temperature. The corresponding diffusion time over 10 Å from the surface is shortened from 60 years for the maximum occupancy to $\sim$ 3 h for smaller occupancies. The flow of SAVs may be facilitated further by short-circuit diffusion along dislocations and/or grain boundaries.

The introduction of SAVs in the near-surface region is expected to become more important in anomalous bcc metals, Fe, V, Nb and Ta, where the diffusivity of vacancies, and hence of Vac-H clusters is so high that their diffusion distance can be much longer than the estimates for fcc metals above. In the case of Nb–H alloys, for example, the diffusivity of a Vac-H cluster was obtained as $D_{\mathrm{cl}} = 10^{-2}\mathrm{e}^{-0.81\mathrm{eV}/kT}\ \mathrm{cm}^2/\mathrm{s}$ [31], which becomes $D_{\mathrm{cl}} = 2.5 \times 10^{-16}\ \mathrm{cm}^2/\mathrm{s}$ at room temperature. The time needed for diffusion over 100 Å is then estimated at 2×10^3 s. Thus in these bcc metals, a near-surface region should be populated with fairly high concentrations of SAVs.

It must be recognized that the SAV formation in the near-surface region should have important implications in hydrogen embrittlement and stress-corrosion processes. As Vac-H clusters in the near-surface region may have concentrations many orders of magnitude higher than vacancies in the absence of hydrogen, they must induce significant changes in the diffusivity of M-atoms and other local mechanical properties. The possibility that M-atom vacancies are playing a key role in hydrogen embrittlement and stress-corrosion were in fact proposed some years ago [32–34], and supporting evidence of enhanced surface diffusion has been provided in some limited cases [35–38]. This is now further substantiated by the discovery and elucidation of SAV formation. Solution of these long-standing problems of materials science appears to be coming in sight.

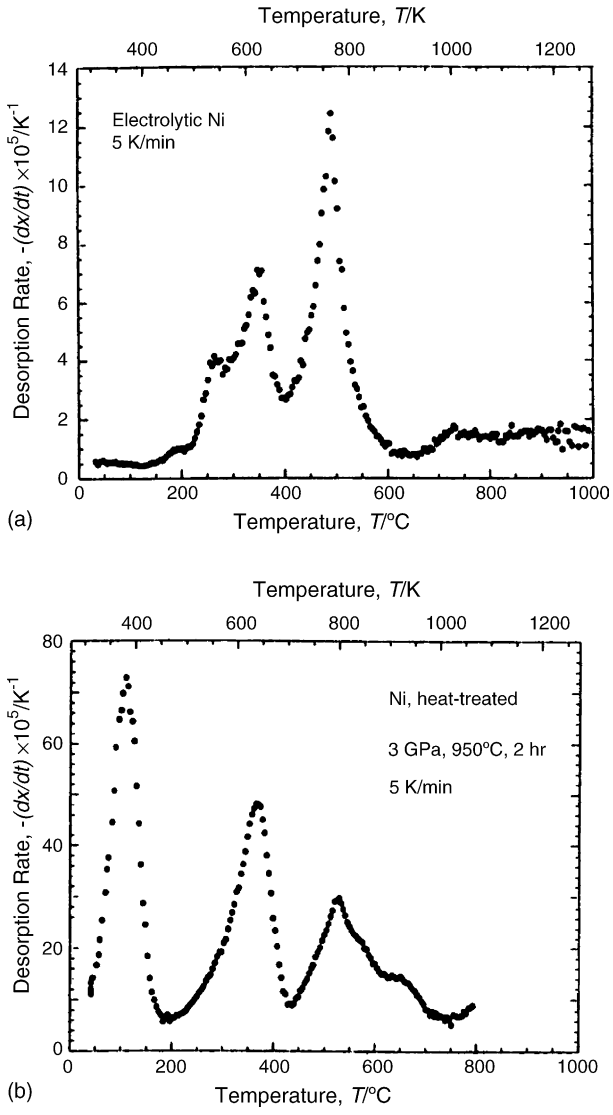

Fig. 16. Thermal desorption spectra of (a) commercial electrolytic Ni after room-temperature ageing over 32 years, (b) a sample recovered from heat treatment at 3 GPa, 950°C for 2 h.

In the electrodeposition process, Vac-H clusters should be introduced more easily, because instead of diffusion in the existing metal lattice, they can be incorporated from the very beginning as one of the constituents of the stable defect structure, atom by atom like laying bricks. Hydrogen atoms introduced in regular interstitial sites during deposition should be lost after recovery to ambient conditions, but those in the form of Vac-H clusters are expected to remain stable.

This expectation was indeed borne out by the results of our TDS measurements. In Fig. 16, the TDS of electrodeposited Ni (a) is compared with the corresponding data on a sample heat treated under high p_H and Ts (b) [2]. The low temperature peak at 150 °C represents the desorption of hydrogen on regular interstitial sites, and the high-temperature peak at 800–1000 °C the desorption of H_2 bubbles. The two peaks at intermediate temperatures (200–400 °C) are identified to be the desorption from Vac-H clusters. The binding energies estimated from these peak temperatures (0.28 and 0.45 eV) are found to agree excellently with those derived from implantation/annealing experiments (0.28 and 0.44 eV) [39].

Perhaps it may be fair to mention that Roy and Gibb [40], trying to explain complex structural properties of electrodeposited Cr films, suggested the formation of defect structures containing M-atom vacancies.

Interestingly, these two peaks were observed in electrodeposited Ni of more than 32 years old! Very similar observations were made on other electrolytic metals as well, including Cr, Cu, Au and Pt. The concentration of SAVs was $\sim 10^{-4}$ in all these cases.

These observations demonstrate that SAVs, once introduced at high chemical potentials, are largely frozen-in at room temperature, and remain as such indefinitely. The implication of this discovery is profound. It not only unraveled the state of hydrogen in electrodeposited metals far in excess of solubility limit—a well-known fact among metallurgists, but also provided a physical basis for investigating the properties of electrodeposited films. Indeed, sluggish changes in alloy structures, enhanced creep processes in electrodeposited films have come to be recognized to be the effect of SAVs.

6. Summary and conclusions

In order to establish a general description of the constitution of metal–hydrogen systems, including their structure and phase relation, experiments were performed over the extended range of chemical potentials. Two methods were adopted for hydrogenation: charging from the gas (fluid) at high p_H, Ts and electrolytic charging (or electrodeposition) at high excess voltages. Some systematics of the phase diagram are shown across the 3d-series M–H alloys, including in particular the reduction of the melting point and stabilization of close-packed structures caused by dissolution of hydrogen.

Structural changes in electrodeposited films were critically examined in Cr, and identified to be the result of hydrogen dissolution.

Implication of SAVs for the phase stability is discussed. In many cases where SAVs can only be introduced by diffusion, their effect is small, and we only have to deal with structures without containing SAVs—meta-stable structures thermodynamically. The exception is the case of anomalous bcc metals (Fe, V, Nb and Ta), where the rapid diffusion may allow the introduction of Vac-H clusters in the near-surface region.

Important effects of SAVs are expected in electrodeposited metals where a defect structure containing SAVs can be built from the very beginning—atom by atom, like laying bricks. SAVs were indeed observed in many electrodeposited metals by thermal desorption spectroscopy. Profound implication of SAVs for many physical properties of electrodeposited films is being recognized.

Properties of M–H systems under high chemical potentials, heretofore conceived of as a special problem under extreme p_H, T conditions, have come to be recognized to have rather general implications including the process occurring in electrodeposition. A new development in this direction is also expected.

References

[1] Y. Fukai, J. Alloys Compd. 356–357 (2003) 263.
[2] Y. Fukai, M. Mizutani, S. Yokota, M. Kanazawa, Y. Miura, T. Watanabe, J. Alloys Compd. 356–357 (2003) 270.
[3] H. Hemmes, A. Driessen, R. Griessen, J. Phys. C 19 (1986) 3571.
[4] H. Sugimoto, Y. Fukai, Acta Metall. Mater. 40 (1992) 2327.
[5] Y. Fukai, The Metal Hydrogen System, Springer, Berlin, 1993 (Chapter 3).
[6] B. Baranowski, in: G. Alefeld, J. Völkl (Eds.), Hydrogen in Metals II, Springer, Berlin, 1978, p. 178.
[7] E.G. Ponyatovskii, V.E. Antonov, in: A.M. Prokhorov, A.S. Prokhorov (Eds.), Problems in Solid State Physics, Mir, Moscow, 1984, p. 108.
[8] V.E. Antonov, J. Alloys Compd. 330–332 (2002) 110.
[9] Y. Fukai, in: M. Doyama, J. Kihara, M. Tanaka, R. Yamamoto (Eds.), Computer Aided Innovation of New Materials II, Elsevier, 1993, p. 451.
[10] Y. Fukai, T. Haraguchi, E. Hayashi, Y. Ishii, Y. Kurokawa, J. Yanagawa, Defect Diffusion Forum 194–199 (2001) 1063.
[11] I.O. Bashkin, E.G. Ponyatovskii, K.E. Kost, Phys. Status Solidi (b) 87 (1978) 369.
[12] P. Vajda, in: K.A. Gschneidner, L. Eyring (Eds.), Handbook on the Physics and Chemistry of Rare Earths, vol. 20, Elsevier, 1995, p. 207.
[13] T.R.P. Gibb Jr., J.J. McSharry, R.W. Bragdon, J. Am. Chem. Soc. 73 (1951) 1753.
[14] Y. Fukai, J. Less-Common Met. 172–174 (1991) 8.
[15] I.O. Bashkin, V.Yu. Malyshev, E.G. Ponyatovsky, Z. Phys. Chem. 179 (1993) 289.
[16] K. Nakamura, Y. Fukai, J. Alloys Compd. 231 (1995) 46.
[17] V. Diatschenko, C.W. Chu, D.H. Liebenberg, D.A. Young, M. Ross, R.L. Mills, Phys. Rev. B 32 (1985) 381.
[18] Y. Fukai, Y. Endo, K. Mogi, T. Hishinuma, Y. Sakamaki, T. Yagi, in press.
[19] Y. Fukai, K. Watanabe, A. Fukizawa, J. Less-Common Met. 88 (1982) 27.
[20] Y. Fukai, M. Mizutani, Mater. Trans. 43 (2002) 1019.
[21] Y. Fukai, T. Haraguchi, H. Shinomiya, K. Mori, Scr. Mater. 49 (2002) 679.
[22] Y. Fukai, K. Mori, H. Shinomiya, J. Alloys Compd. 348 (2002) 105.
[23] Y. Fukai, J. Yanagawa, S. Yokota, in press.
[24] Y. Shizuku, S. Yamamoto, Y. Fukai, J. Alloys Compd. 336 (2002) 159.
[25] Y. Fukai, S. Yamamoto, S. Harada, M. Kanazawa, J. Alloys Compd. 372 (2004) L4.
[26] T. Hiroi, Y. Fukai, K. Mori, J. Alloys. Compd. 404–406 (2005) 252–255.
[27] T. Watanabe, Nano-Plating—Microstructure Formation, Elsevier, 2004.
[28] Y. Miura, S. Yokota, Y. Fukai, T. Watanabe, Mater. Trans. 46 (2005) 963.

[29] Y. Fukai, Y. Ishii, Y. Goto, K. Watanabe, J. Alloys Compd. 313 (2000) 121.
[30] P. Ehrhart, P. Jung, H. Schultz, H. Ullmaier, in: H. Ullmaier (Ed.), Atomic Defects in Metals, Landolt-Börnstein, New Ser., vol. 25, Springer, 1991.
[31] H. Koike, Y. Shizuku, A. Yazaki, Y. Fukai, J. Phys.: Condens. Matter 16 (2004) 1335.
[32] M. Nagumo, ISIJ Int. 41 (2001) 590.
[33] J.R. Gavele, Corros. Sci. 35 (1993) 419.
[34] J.R. Gavele, in: R.E. White et al., (Eds.), Modern Aspects of Electrochemistry, vol. 27, Plenum, New York, 1995, p. 233.
[35] Z.R. Xu, R.B. McLellan, Scr. Mater. 39 (1998) 365.
[36] N. Hirai, H. Tanaka, S. Hara, Appl. Surf. Sci. 130–132 (1998) 506.
[37] R. van Gastel, E. Somfai, W. van Saarloos, J.W.M. Frenken, Nature 408 (2000) 665.
[38] R. van Gastel, E. Somfai, S.B. van Albada, W. van Saarloos, J.W.M. Frenken, Surf. Sci. 521 (2002) 10.
[39] S.M. Myers, P. Nordlander, F. Besenbacher, J.K. Nørskov, Phys. Rev. B 33 (1986) 851.
[40] R.J. Roy, T.R.P. Gibb Jr., J. Inorg. Nucl. Chem. 29 (1967) 341.